Journal of Renewable and Sustainable Energy

AIP Publishing

RESEARCH ARTICLE | NOVEMBER 21 2024

Estimating the offshore wind power potential of Portugal by utilizing gray-zone atmospheric modeling

H. Baki ; S. Basu ; G. Lavidas

J. Renewable Sustainable Energy 16, 063306 (2024)
https://doi.org/10.1063/5.0222974

Articles You May Be Interested In

A comparative study of soiling on solar mirrors in Portugal and Morocco: Preliminary results for the dry season

AIP Conf. Proc. (July 2019)

Forecasting Portugal's Wind Power Production by a Fuzzy-PCA Approach

AIP Conf. Proc. (September 2011)

How electricity generation regimes are interacting in Portugal. Does it matter for sustainability and economic activity?

J. Renewable Sustainable Energy (March 2016)

Journal of Renewable
and Sustainable Energy
ARTICLE
pubs.aip.org/aip/rse

Estimating the offshore wind power potential of Portugal by utilizing gray-zone atmospheric modeling

Cite as: J. Renewable Sustainable Energy **16**, 063306 (2024); doi: 10.1063/5.0222974
Submitted: 11 June 2024 · Accepted: 12 October 2024 ·
Published Online: 21 November 2024

H. Baki,[1,a)] S. Basu,[2,3] and G. Lavidas[4]

AFFILIATIONS

[1] Faculty of Civil Engineering and Geosciences, Delft University of Technology, Delft, The Netherlands
[2] Atmospheric Sciences Research Center, University at Albany, Albany, New York 12226, USA
[3] Department of Environmental and Sustainable Engineering, University at Albany, Albany, New York 12226, USA
[4] Faculty of Civil Engineering and Geosciences, Marine Renewable Energies Lab, Delft University of Technology, Delft, The Netherlands

[a)] Author to whom correspondence should be addressed: h.baki@tudelft.nl

ABSTRACT

Advancements in floating offshore wind energy are unlocking the potential of the coastal waters of Portugal for the installation of wind farms. A thorough evaluation of coastal effects and variability across different time scales is crucial to ensure successful offshore wind farm investments. State-of-the-art atmospheric reanalysis datasets fall short in explaining the coastal effects due to their modest grid resolution. This study aims to fill this gap by simulating a 31-year wind dataset at a gray-zone resolution of 500 m using the Weather Research and Forecasting model, covering a significant portion of the Portugal coast. The gray-zone refers to grid scales of a few hundred meters, where turbulence is only partially resolved, traditional turbulence modeling breaks down, and large-eddy simulations are computationally prohibitive. The newly generated dataset has been validated with buoy observations and compared against reanalysis datasets, demonstrating improved performance and highlighting its higher fidelity in assessing wind resources. Two wind turbine power curves, the Leanwind 8 megawatt (MW) reference wind turbine (RWT), which has been commercialized, and the International Energy Agency (IEA) 15 MW RWT, which represents future commercialization, are considered in energy production calculations. In the simulated data, the Iberian Peninsula Coastal Jet (IPCJ) emerges as a crucial factor influencing wind maxima, especially during the summer months. The diurnal and annual variability of wind energy resources aligns with the occurrence of IPCJ, highlighting its impact on wind energy generation. The energy production capability of the 15 MW turbine model is demonstrated to be significantly higher, attributed not only to its increased capacity but also to the stronger jet winds near the turbine hub height. Interestingly, wind resources are not monotonically increasing with distance from the coastline, but a tongue-like resource maxima is observed, which is attributed to the IPCJ.

I. INTRODUCTION

Global reduction of fossil fuel reserves, as well as increasing awareness of human impact on climate change, has significantly contributed to the acceleration in the deployment of renewable energy technologies. Consequently, the European Union has set ambitious targets of 32% renewable energy sources by 2030 and to achieve a net reduction of Greenhouse gas emissions by at least 55%.[1] Offshore wind energy stands out as a promising avenue for attaining these objectives, primarily for two compelling reasons. First, offshore wind resources are abundant and carry higher energy fluxes due to, among others, reduced surface roughness allowing higher wind speeds. Second, technological advancements have enabled the deployment of the largest wind turbines to date, exemplified by the MySE 16-260,[2] boasting a 16 MW capacity, 260 m rotor diameter, and 152 m hub height, thus facilitating the harnessing of abundant winds at higher altitudes. Moreover, new methods of deploying the turbines far offshore, such as floating wind turbines, have effectively eliminated the constraints associated with proximity to the shore, enabling the exploitation of extensive wind resources in deep offshore locations.[3]

Portugal stands out as a country benefiting significantly from the development of floating offshore wind farms. This is predominately due to the larger ocean depths in Portuguese waters compared to other Northern European countries, which make the construction of fixed-bottom offshore wind farms less feasible.[4] Portugal's commitment to the development of offshore wind energy is evidenced by the establishment of Europe's first offshore semi-submersible floating wind farm, WindFloat Atlantic, with a capacity of 25 MW and three turbines. Operational since July 2020, it had already generated a cumulative total of 180 GWh by the end of 2022.[5] Building on this success, the Portuguese government has conducted auctions for a substantial 10 GW of offshore wind capacity to be developed by the end of 2030. As a result, numerous projects are currently in various stages of development or planning. Notable examples include Viana do Castelo north (1010 MW), Viana do Castelo south (990 MW), WavEC (2 MW), Leixoes (1500 MW), Figueira da Foz (4000 MW), and Ericeira (1000 MW). While the benefits of harnessing offshore wind resources in Portugal are evident, it is crucial to recognize that the costs associated with offshore wind energy development are considerably higher. Consequently, conducting precise assessments of wind resources at potential turbine construction sites becomes increasingly essential to ensure the viability and success of these projects.[6,7]

Coastal effects in the atmosphere result from differences between the physical properties of land and ocean surfaces, with two main factors at play: ocean surfaces exhibit lower roughness length scales compared to land, while ocean water possesses a significantly greater heat capacity than typical soil. Among many, some of the well-known phenomena are internal boundary layers (IBLs), coastal low-level jets (LLJs), and sea breezes, which have been shown to influence wind farms, as discussed in a number of studies in the past.[8–10] In addition, sea surface roughness differs between open ocean and coastal regions, suggesting the influence of coastal wind gradients and waves. A review conducted by Schulz-Stellenflet *et al.*[11] underscores the importance of considering a wide range of spatial and temporal scales when assessing the coastal effects on offshore wind farms.

With ever growing sizes of wind turbines with hub heights reaching 150 m, accurate characterization of wind resources at this level is of paramount importance. Typically, the primary means for acquiring reasonable long-term wind data at higher altitudes involve wind masts, SODAR, and LiDAR.[12–14] While these sources offer certain advantages, including accurate measurement at a high temporal frequency, they are often expensive to install in deep waters and sparsely distributed, making them inadequate for detailed spatial wind monitoring. Instead of vertically pointing, a lidar can also be used in horizontal scanning mode, in which the lidar beam sweeps the atmosphere in azimuth from 0 to 360, at various elevations, creating a three-dimensional conical dataset.[15] Such lidars can offer insight into the spatial variability of wind patterns. However, they are very expensive to install, and their horizontal range is typically limited to a few kilometers.

Consequently, the atmospheric reanalysis proven to be a great alternative for offshore wind resource assessment, particularly due to their spatiotemporal coverage.[16] Several researchers have utilized global and regional reanalysis datasets, such as the ECMWF-Re-Analysis Interim (ERA-Interim),[17] the Modern-Era Retrospective Analysis for Research and Applications version 2 (MERRA-2),[18] and the fifth generation ECMWF atmospheric reanalysis (ERA5),[19] in addressing the spatiotemporal variability of offshore wind resources, as well as in understanding the influence of atmospheric circulation patterns on wind power production.[16,20] However, the coarse resolution of reanalysis data is inadequate in capturing coastal effects.[11] For example, the current state-of-the-art regional reanalysis, Copernicus Regional Reanalysis for Europe (CERRA),[21] has a limited resolution of 5.5 km.

In tackling these limitations, mesoscale atmospheric models, particularly the Weather Research and Forecasting (WRF) model, offer a cost-effective solution, providing much higher spatial and temporal resolution than reanalysis datasets. A comprehensive list of the studies conducted wind resource assessment over Portugal using the WRF model is presented in Table I, along with some configuration details.

Carvalho *et al.*[22] conducted a series of sensitivity experiments using the WRF model, with different initial and boundary conditions, for 1 year, at 5 km grid resolution, over the Iberian coast. The authors concluded that the WRF model forced with the ERA-Interim data offers better offshore wind simulations and has proven to be a good alternative for generating offshore wind data with extensive spatiotemporal coverage where the observations are scarce. The authors followed up with several studies to estimate the offshore wind resources over the Iberian coast.[23–26,28] From these studies, it is clearly evident that initial and boundary conditions, a combination of planetary boundary layer and surface layer physics parameterization, and grid resolution play a vital role in improving the simulation accuracy.

Salvação and Guedes Soares[27] conducted a detailed offshore wind resource assessment over the Iberian coast, using two simulation configurations: one with 9 km resolution for 10 years of simulations and another with 3 km resolution for 6 months of simulations. The authors concluded that a minimum of 10 years of climate information is essential for accurate wind resource assessment. Around the same time, Couto *et al.*[30] conducted a series of sensitivity experiments to ascertain the best combination of initial and boundary conditions, physics options, and the assimilation strategy using the Fifth-Generat Penn State/NCAR Mesoscale Model (MM5). With the obtained calibrated setup, they generated three years of high-resolution offshore wind atlas for the Portugal coast, with a grid resolution of 1 km. In a more recent work, Plecha *et al.*[29] simulated 44 years of ocean surface winds at a resolution of 3 km over the Portugal coast, evaluated their accuracy against satellite winds, and concluded that the WRF model is the best choice for generating high resolution spatiotemporal ocean wind datasets with good accuracy in terms of capturing trends and other statistics.

It is evident that past modeling studies suffered from one of two limitations. In some cases, the spatial resolutions were reasonably high, but the simulation durations were insufficient to capture inter-annual and annual variabilities. In other studies, which involved multi-year simulations, the spatial resolution was too coarse to reliably capture coastal effects.

Recently, the Japanese offshore wind atlas developed by the New Energy and Industrial Technology Development Organization (NEDO), NEDO Offshore Wind Information System (NeoWins),[31] employed 500 m gray-zone resolution for coastal waters up to 30 km from the coastline to retrieve complex wind conditions of the Japanese coast. The dataset demonstrates the need for gray-zone resolution resource assessments in coastal regions to support the ever-growing offshore wind industry. Building upon this idea and considering the aforementioned limitations, the present study has generated a 31-year wind dataset at a resolution of 500 m using the WRF model over a significant region of Portugal's coast.

TABLE I. A comprehensive list of studies conducted wind resource assessment over the Portugal coast using the WRF model.

Study	Grid size	Simulation duration	PBL scheme
22–25	5 km	1 year	The Yonsei University (YSU) scheme
26	5 km	1 year	YSU scheme, the Mellor-Yamada-Janjic (MYJ) scheme, the Asymmetric Convective Model version 2 (ACM2) scheme, the Quasi-Normal Scale Elimination (QNSE) scheme, and the Mellor-Yamada Nakanishi and Niino level 2.5 (MYNN-2.5) scheme
27	9 and 3 km	10 years with the 9 km grid and 6 months with the 3 km grid	YSU scheme
28	6 km	20 years	YSU scheme
29	3 km	44 years	YSU scheme

In traditional mesoscale model simulations, the horizontal grid size (order of 1 km or coarser) is much larger than the energy containing turbulent eddies. As a result, turbulence is not resolved, and it is fully parameterized by a planetary boundary layer (PBL) scheme. This scheme is used in conjunction with the Reynolds-averaged Navier–Stokes (RANS) equations. Since the vertical gradients are much larger than the horizontal ones in typical mesoscale modeling, the PBL schemes are usually one-dimensional and only captures vertical turbulent exchanges. In the case of atmospheric simulations with sub-kilometer grid spacing, turbulence is partially resolved, and as a consequence, the inherent assumptions of the RANS modeling break down. If the grid spacing is on the order of a few meters, one can perform large-eddy simulations. For intermediate grid spacing (e.g., a few hundred meters), one must opt for a gray-zone parameterization.[32–36] For such simulations, the use of traditional PBL schemes is not recommended. Given the widespread access of high-performance computing resources in recent years, sub-kilometer modeling is gaining popularity in wind energy literature; however, most of these studies are incorrectly using traditional PBL schemes. For examples, Jiménez *et al.*[37] conducted WRF model simulations with a grid spacing of 333 m for offshore wind farm modeling but failed to acknowledge the gray-zone limitation.

The present study documents wind resource assessment at the Portugal coast with sub-kilometer (500 m) resolution using an appropriate gray-zone PBL parameterization. In addition, two turbine power curves, an 8 MW model with a hub height of 120 m currently employed in coastal waters, and a state-of-the-art 15 MW model with a hub height of 150 m representing future developments in offshore wind technology, are utilized. Impacts of the higher resolution dataset are evident in power production, and the identification of physical phenomena, such as the IPCJ, which given consequential for power production. Our unique dataset also assesses the resource variability at diurnal, interannual, and annual scales provides additional insights into the suitability of the mesoscale models for capturing the dynamic nature of offshore wind resources and the importance of physical effects noticeable only at sub-kilometer scales.

II. DATA AND METHODOLOGY

A. Model description and simulation design

In the present study, the WRF model (version 4.4)[38] is adopted for numerical simulations. The offshore wind resource assessment is primarily focused on the parts of Portugal's coast adjacent to the districts Viana do Castelo, Braga, and Porto, where several wind farms are slated for development. The interested area spanned between the coordinates (41.286°N, 9.3472°W) and (41.7558°N, 8.7307°W), encompassing an approximate area of 3600 square km. The farthest distance from the coast within this region is 45 km. Accordingly, the WRF model has been configured with a single domain, at 500 m resolution, encompassing the interested area as shown in Fig. 2(a), which is a main focus of the European Green Deal project EU-SCORES (https://cordis.europa.eu/project/id/101036457). This domain is termed as SCORES domain, hereafter. Within the domain, the existing WindFloat Atlantic (WFA) offshore wind farm is located with a purple star.

Table II presents the WRF model configuration and physics schemes utilized in this study, in which the Shin-Hong PBL scheme is a gray-zone parameterization has been designed to address the turbulence transport issue at sub-kilometer grid scale. The CERRA data, available at 5.5 km spatial resolution and temporal resolution of 3 h, have been utilized as initial and boundary conditions for the numerical experiments. Despite the advantages of CERRA, the data have never been used as forcing data for mesoscale simulations and not been incorporated into the WRF model configuration. In a previous study,[39] we developed the methodology to incorporate the CERRA reanalysis. The same has been adopted in this study for ingesting the CERRA reanalysis into the WRF model. A total of 31 years (1990–2020) of numerical simulations are conducted using the SCORES domain configuration ($\mathrm{WRF_{SCORES}}$), such that the simulations are reinitialized at 0000 UTC every 5 days and run for 6 days. After excluding the first 24-h spin-up time, the simulated outputs from the 5-day periods are considered for analysis. In this design, 2265 runs are performed to cover the entire 31-year period. A detailed illustration of the methodology is presented as a flow chart in Fig. 1.

The $\mathrm{WRF_{SCORES}}$ domain does not contain any observational stations. However, there are a few stations which are located outside this

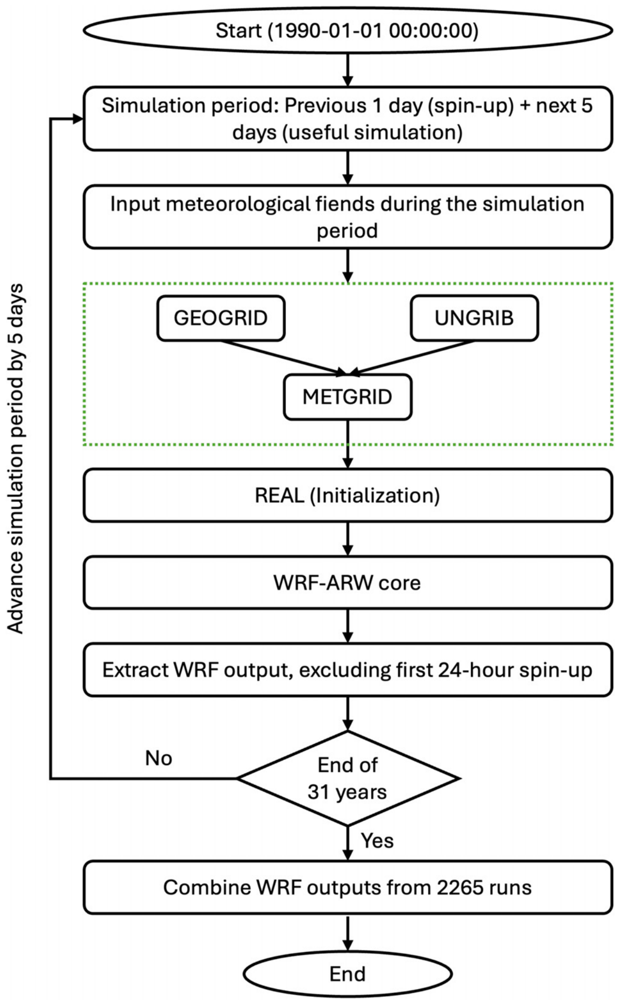

FIG. 1. Flowchart of the WRF simulations conducted using the SCORES domain. The simulations start on 1990-01-01 00:00:00 and continue in a retrospective mode by an increment of 5 days, until the end of 2021-01-01 00:00:00, totaling 2265 WRF runs.

domain as shown in Fig. 2(b). In order to assess the quality of the simulations, we decided to run additional 1-year long simulations using an Extended domain (WRF_{Ext}). These experiments also follow a similar strategy adopted for the SCORES domain simulations, but starting from 2011-07-01 00:00 and ending at 2012-07-01 00:00, with a similar recursive strategy. Due to exorbitant computational cost, we were unable to extend these simulations beyond a duration of 1 year.

B. Observational and reanalysis data

Wind observations used for the model validation were collected from three coastal marine buoys, namely, A Guarda, Cies, and Cabo Silleiro (CS). Table III provides important information about the buoys, while the locations of these buoys are illustrated in Fig. 2. Wind measurements taken from the 1st of July 2011 to the 1st of July 2012 (1 year) were selected, and the choice of this period was related to measured data availability and quality criteria. Though the data are measured at every 10 min, they are available at hourly frequency averaged of each hour. The buoys considered in this study collect measurements at 3 and 4.5 m above sea level (asl), necessitating extrapolation to near surface ocean wind level, typically 10 m asl. Traditional methods like the Monin–Obukhov similarity theory require additional data (e.g., two-level wind speed, two-level temperature, or measured sensible heat fluxes), which are unavailable from these buoys. In the absence of essential data, and based on the studies of Refs. 25 and 44, a simplified logarithmic wind profile expression (1) is adopted for extrapolation from the observed height to 10 m asl.

TABLE II. WRF model configuration and parameterization options.

Horizontal resolution	500 m
Grid dimension	128×128 ($\text{WRF}_{\text{SCORES}}$) 165×240 (WRF_{Ext})
Vertical levels	51
Terrain resolution	30 s
Radiation parameterization	RRTMG for shortwave and longwave[40]
PBL parameterization	Shin-Hong[35]
Surface layer parameterization	Revised MM5[41]
Land surface parameterization	Unified NOAH[42]
Microphysics	WRF single moment 5-class[43]

$$U_Z = U_{Z_m} \frac{\ln\left(\frac{Z}{z_\circ}\right)}{\ln\left(\frac{Z_m}{z_\circ}\right)}. \tag{1}$$

Here, U_Z refers to the wind speed at a height Z, Z_m is the measurement height (e.g., 3 m asl), and $z_\circ$ is the local roughness length. Earlier studies[25,44] suggested that a roughness length of 0.0002 m is appropriate for open ocean surface, and the same has been adopted in this study. We do note that the assumption of constant roughness is not appropriate for areas close to the coastline (i.e., in and around surf-zones); however, it can be used as a reasonable approximation for far offshore areas (e.g., at the WFA wind farm site). We also acknowledge that the logarithmic law assumes a neutrally stratified atmosphere and disregards the effects of atmospheric stability. To support the applicability of the expression for our specific area of interest, we looked into the surface sensible heat flux from ERA5 as a proxy to the atmospheric stability, near the CS buoy cite, as shown in Fig. 3. From the distribution, it is evident that 71% the sensible heat flux lies with in the ± 10 W/m^2 range. In other words, more than two-thirds of the cases are close to near-neutral.[45] So, we expect errors are not to be large between measured and extrapolated wind speeds, and thus, we proceed with the logarithmic law for extrapolation.

Apart from the observations, two reanalysis datasets, namely, ERA5[19] and CERRA were also used for the model validation. Published in 2019, ERA5 is the 5th generation European Center for Medium-Range Weather Forecasts (ECMWF) reanalysis dataset, stands as the most recent iteration among the ECMWF global reanalysis products. It provides hourly estimates for various variables, with a spatial resolution of approximately 31 km (0.25° × 0.25°) and covers

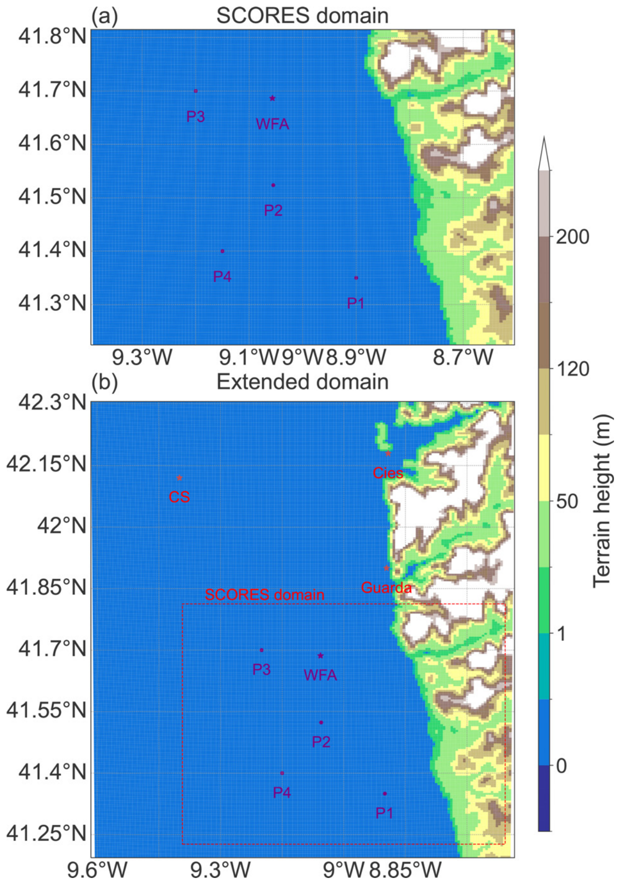

FIG. 2. WRF model domain configurations: (a) SCORES domain for 31-year hindcast simulations (1990-01-01 to 2021-01-01); (b) Extended domain for 1-year validation simulations (2011-07-01 to 2012-07-01). Three coastal buoys are shown with stars in (b). In both figures, the WindFloat Atlantic (WFA) offshore wind farm is located with a purple star, while four random points, P1, P2, P3, and P4, are illustrated with purple solid circles. These five points are utilized in sensitivity with respect to domain size and resource assessment analysis.

137 vertical levels up to 0.01 hPa. The dataset spans from 1940 to the present, offering comprehensive information that includes wind speed, not only at the standard 10 m level seen in its predecessors but also at the elevated 100 m level. Several studies[16,46,47] discuss ERA5's superior accuracy, lower uncertainty, and higher reliability compared to other global reanalysis datasets.

Released in 2022, the Copernicus Regional Reanalysis for Europe (CERRA)[21] is a state-of-the-art reanalysis dataset, down-scaled from the ERA5 reanalysis, and developed by the collaborative efforts of the Swedish Meteorological and Hydrological Institute (SMHI), Norwegian Meteorological Institute (MET Norway), and Meteo-France. CERRA provides a high-resolution pan-European reanalysis with a 5.5 km horizontal resolution, three-hourly temporal resolution, and 106 vertical levels, covering Europe, Northern Africa, and Southeastern parts of Greenland. Unlike any other reanalysis, this dataset also offers wind speed and many other variables at different model levels, ranging from 10 to 500 m.

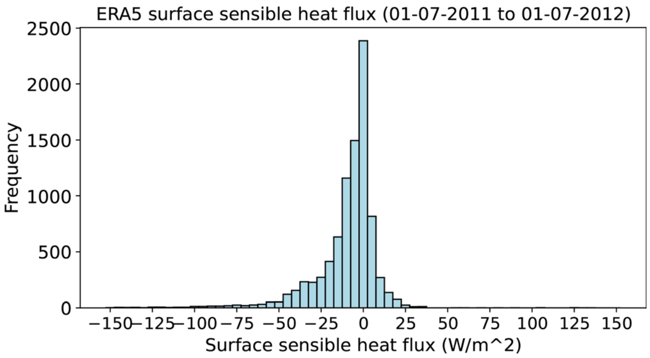

FIG. 3. Histogram of surface sensible heat flux from ERA5 reanalysis near the CS buoy cite, during 1st of July 2011 to the 1st of July 2012 (1 year).

III. MODEL VALIDATION AND SENSITIVITY

A. Validation against observations

Before the model can be considered a reliable tool for assessing wind resources, a thorough evaluation against observational data becomes imperative. For this purpose, the WRF_{Ext} simulations conducted over a 1-year period using an extended domain undergo scrutiny employing various assessment methods. The Bias quantifies the tendency of the simulations, toward overprediction or underprediction compared to the observations. The root mean square error (RMSE) quantifies the square root of the average squared differences between model predictions and corresponding observations, providing insight into the magnitude of errors. Pearson's correlation coefficient (r) assesses the linear relationship between model and observed values. The scatter index (SI) normalizes model performance against the scale of observed data by comparing RMSE to the mean observed value. The mean absolute error (MAE) quantifies the magnitude of the error in simulations with respect to the observations. The standard deviation error (STDE), introduced by Carvalho *et al.*,[48] measures the consistency of error in model simulations. Even when a model shows high RMSE or Bias, a low STDE suggests that the model's physics are sound, and the error can be interpreted as a systematic offset. In

TABLE III. Some important features of the marine buoys used in this study.

Name	Location	Distance to shore (km)	Height (m)	Sampling rate (min)	Programme	Period	WMO number
A Guarda	41.9° N, 8.896° W	1.5	4.5	60	Xunta de Galicia	29-07-2010 to 30-09-2022	6201031
Cies	42.179° N, 8.892° W	1.2	4.5	60	Xunta de Galicia	04-04-2008 to 30-09-2022	6201040
Cabo Silleiro	42.12° N, 9.4° W	40	3	60	Puertos del Estado	06-07-1998 to present	6200084

contrast, a high STDE implies that the error is more random, reducing the physical reliability of the simulation, even if the RMSE or Bias appears low. Furthermore, the data from ERA5 and CERRA are also evaluated with respect to the observations to examine the similarity between the WRF simulations and the reanalysis, providing a comprehensive validation of the model's performance against multiple datasets.

Figure 4 illustrates bivariate histograms and wind roses of 10 m wind speeds and direction from ERA5, CERRA, and the WRF_{Ext} simulations at three buoy sites (Guarda, Cies, and CS), compared with observations. These datasets cover a period of 1 year, from 01-07-2011 to 01-07-2012. It is noteworthy to mention that buoy locations, Guarda and Cies, are within 1.5 km from the shore, while CS lies at a distance of 40 km offshore. Winds at the Guarda and Cies locations are expected to be significantly influenced by coastal boundaries. Additionally, wind patterns are affected by variations in surface roughness within the surf zone (the area near the shore where waves break) due to factors such as viscous smooth flow roughness, aerodynamic roughness from wave form drag and flow separation, and roughness caused by spray droplets and foam.[49] Wind direction also plays a critical role in roughness length: winds perpendicular to the coast (onshore winds) typically generate higher roughness and lower wind speeds due to wave steepening, while winds parallel to the coast often result in much lower roughness and higher wind speeds, especially at lower wind speeds, possibly due to coastal upwelling and short fetch distances leading to lower wave heights.[50]

The ERA5 dataset appears to largely underestimate wind speeds at these two locations, as evident from the significant biases (−2.78 m/s at Guarda, −1.14 m/s at Cies, and 1.29 m/s at CS) observed. Furthermore, the ERA5 data show a limitation in reproducing winds exceeding 13 m/s near coastal boundaries, while observed winds reach up to 20 m/s. In contrast, bivariate histograms of wind speeds from CERRA and the WRF_{Ext} simulations are comparable, with WRF_{Ext} marginally performing better by reducing the bias (−0.89 m/s at Guarda, 0.13 m/s at Cies, and 1.21 m/s at CS).

At the Guarda location, the histograms from the three datasets exhibit a secondary distribution with significant biases as mentioned. A wind rose comparison revealed two prevailing wind directions in the observed data, one coming from the north (0°) and another from the east (90°). While the northerly winds are well captured by all three datasets, both ERA5 and CERRA failed to represent the easterly winds, a phenomenon solely reproduced by the WRF_{Ext} simulations. To investigate whether this discrepancy is the root cause of the secondary distribution observed in the bivariate histograms, we isolated winds blowing from the east. Gaussian distributions were fitted to these easterly winds and are depicted as red dashed ellipses in Fig. 4. It was discovered that indeed, the easterly winds were the source of the observed discrepancy. From the figure, it is evident that WRF_{Ext} significantly improved the simulation of easterly winds, with the Gaussian ellipse oriented more toward the 45° line, in contrast to ERA5 and CERRA. On the other hand, the wind rose diagram at the Cies location shows that the wind directions are well distributed to all sectors. At this location too, the WRF_{Ext} simulations closely following the observed wind directions, while the ERA5 and CERRA are showing visible deviations.

Although the Guarda and Cies locations are in close proximity to the shore, and are separated by no more than 15 kilometers to one another, a significant disparity in wind speed and direction exists between these two sites. To comprehend the physics behind this difference, we examined the geographical terrain. Guarda is obstructed by steep topography to the east. Consequently, winds coming from the west experience a reduction in speed, while land breezes from the east strengthen, due to the down slope wind. Winds blowing from the south and north have unrestricted movement, but northerly winds are notably stronger at this location. Conversely, the Cies buoy is situated in a channel extending from northwest to southeast, obstructed by a small island in the north and steep topography in the south. As a result, northeasterly and southwesterly winds dominate at this location. Since the WRF_{Ext} simulations are configured with a 500 m grid resolution, they are well capable of resolving the steep topography and thereby land-sea interactions, which resulted better wind speed simulations at these two locations.

Finally, the CS buoy is located far offshore, where the three datasets exhibit good agreement with observations, reflected in a Pearson's correlation coefficient of around 0.9. The WRF_{Ext} simulations outperform ERA5 and CERRA, showcasing reduced Bias (1.21 m/s), RMSE (1.91 m/s), MAE (1.48 m/s), and SI (36.66%). Though the ERA5 is marginally better in terms of the STDE (1.42 m/s), the WRF_{Ext} simulations also exhibit a similar STDE of 1.48 m/s, implying that the model simulations are physically valid. Additionally, the wind directional distributions depicted in the wind rose indicate that the WRF_{Ext} simulations effectively capture the northerly winds prevalent at this location.

The aforementioned traditional metrics provide valuable insights into model accuracy, but may overlook the significance of subtle changes in the shape of the wind speed distribution. In wind energy applications, where wind power density is proportional to the cube of wind speed, small variations in the distribution can have a pronounced impact on power generation. To address this limitation, the earth mover's distance (EMD)[51] is introduced as a metric that evaluates differences in the shape of frequency distributions, which has been referred to as various names: transportation distance, Kantorovich metric, Wasserstein metric, Hutchinson metric, etc. The EMD can be interpreted as the amount of physical work needed to move a pile of soil in the shape of one distribution to that of another distribution, making it particularly relevant for applications where the shape of the distribution is crucial, such as wind resource assessments and estimates in power production.[52] The EMD calculated using the python scipy stats package, a lower value indicates close resemblance between the frequency distributions, while a higher value indicates otherwise. Figure 5 illustrates the 10 m wind speed distributions from the three datasets in comparison with buoy observations at the three observational locations, along with the EMD estimates.

At the Guarda location, the observed distribution extends over a considerable range, centered around a mode of 5 m/s. In contrast, at the Cies location, the distribution skews to the left, centering around a mode of 3 m/s. At both locations, ERA5 exhibits a skewed distribution centered around a mode of 3 m/s. It significantly underestimates wind speed frequencies beyond 7 m/s, while overestimating frequencies around 3 m/s. These observations align with the large negative biases estimated earlier. CERRA and WRF_{Ext} simulations present similar wind speed distributions at the Guarda location. They underestimate high wind speed frequencies and overestimate low wind speed frequencies, with the WRF_{Ext} distribution slightly aligning better with the observed one. This alignment is consistent with the negative biases observed earlier, where WRF_{Ext} simulations perform slightly better. In

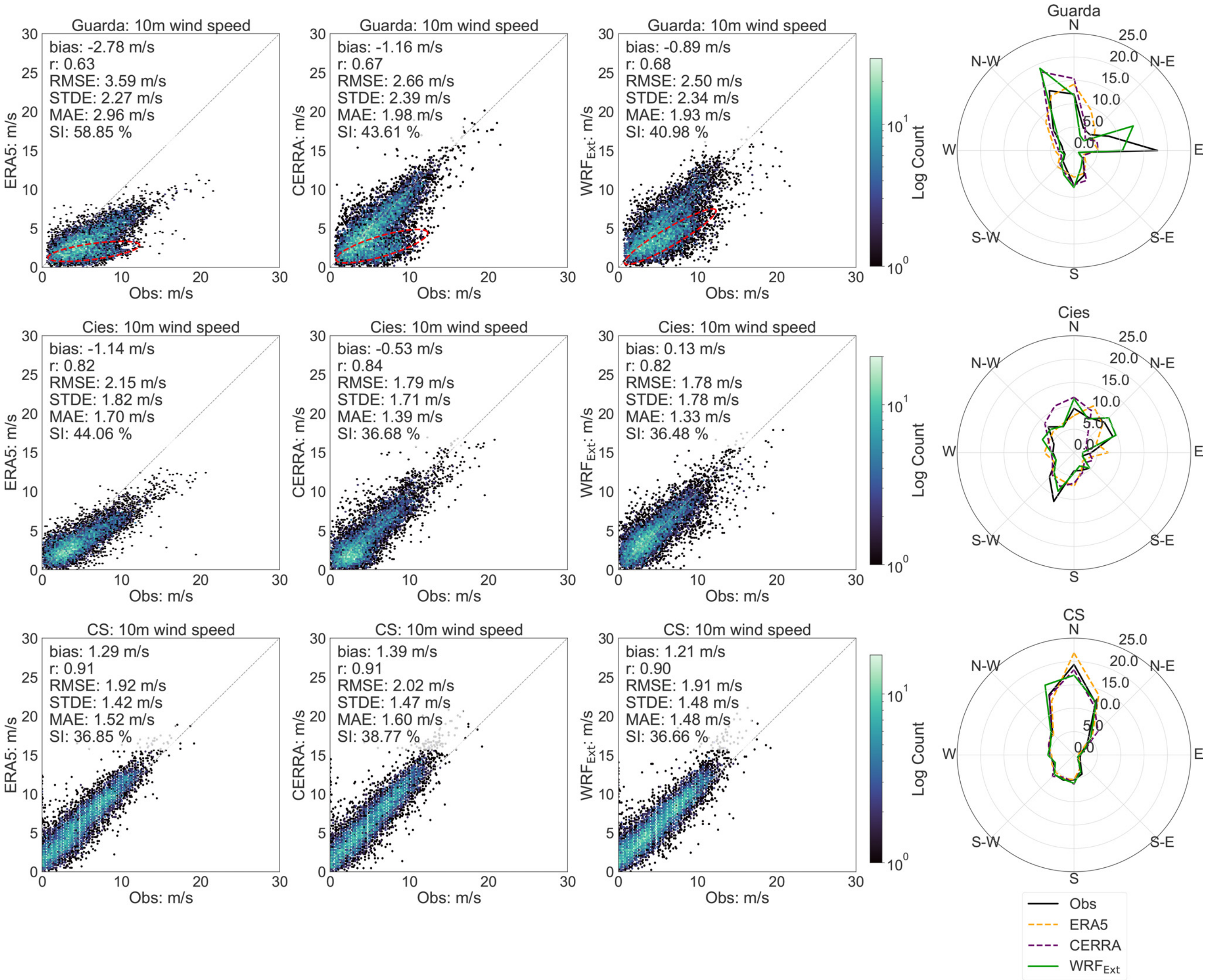

FIG. 4. Bivariate histograms depicting the 10 m wind speed distribution from ERA5 (first column), CERRA (second column), and WRF$_{Ext}$ simulations (third column), compared with three buoy observations: Guarda (first row), Cies (second row), and CS (third row). The number of occurrences is presented in log count, with darker (lighter) color indicating low (high) occurrence. The red dashed ellipses shown in Guarda subfigures are explained in the main text. The evaluation statistics including Bias, RMSE, Pearson's correlation (r), standard deviation error (STDE), mean absolute error (MAE), and the scatter index (SI) are computed to assess the agreement between the three datasets and observational data. Additionally, the wind roses (fourth column) illustrate the comparison of 10 m wind direction among the four datasets, buoy observations, ERA5, CERRA, and WRF$_{Ext}$ simulations, at the three buoy locations Guarda (first row), Cies (second row), and CS (third row). The data span a collection period from 01-07-2011 to 01-07-2022, covering a year-long duration.

contrast, at the Cies location, the CERRA distribution shifts to the left of the observed one, overestimating low wind frequencies and underestimating high wind frequencies. Meanwhile, the WRF$_{Ext}$ distribution shifts to the right of the observed one, overestimating high wind frequencies and underestimating low wind frequencies. These shifts are in line with the negative bias for CERRA and positive bias for WRF$_{Ext}$ observed earlier. At these two locations, ERA5 is observed to have a higher EMD value, indicating significant dissimilarity with respect to the observed distribution. In contrast, WRF$_{Ext}$ is found to have a lower EMD value, implying better agreement with the observed distribution.

At the CS location, observations reveal a wider distribution with two peaks, one at 3 m/s and another at 7 m/s. The distributions from ERA5, CERRA, and WRF$_{Ext}$ also exhibit bimodal peaks and consistently shift to the right of the observed one, implying an overestimation of all wind speed frequencies. Notably, the WRF$_{Ext}$ distribution is slightly closer to the observed one during high wind speeds, leading to the reduction in wind speed bias, as observed earlier. At this location, the CERRA distribution is noted to have a higher EMD value, while the WRF$_{Ext}$ distribution has the least EMD value, indicating better agreement of the WRF simulations with observations. The WRF$_{Ext}$ simulations consistently exhibit better agreement with observed wind

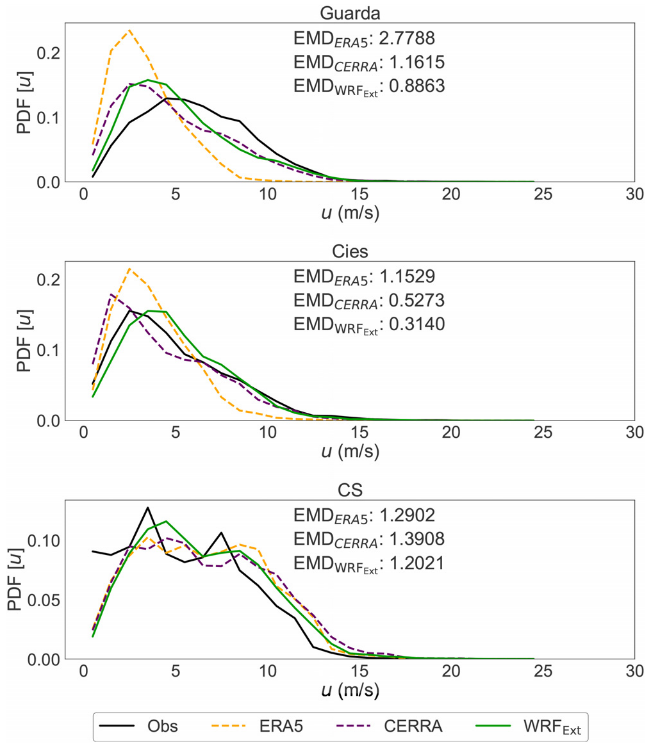

FIG. 5. Comparison of 10 m wind speed distributions from ERA5, CERRA, and WRF$_{Ext}$ datasets, with respect to the buoy observations, at locations: Guarda (first row), Cies (second row), and CS (third row). The EMD is calculated and shown, assessing dissimilarities between the datasets and observational data.

patterns, suggestion improved performance for precise wind resource assessments.

B. Sensitivity with respect to domain size

So far, we have assessed the accuracy of the WRF$_{Ext}$ simulations, covering the observational period from 01-01-2011 to 01-01-2012. Since our primary focus has been on wind resource assessment for 31 years using the WRF$_{SCORES}$ simulations, no tall tower observational data are available within this domain to validate the simulations. In light of this and prove the better agreement between WRF$_{Ext}$ and observations seen earlier, we have no choice but to utilize WRF$_{Ext}$ simulations as a reference to evaluate the accuracy of WRF$_{SCORES}$ simulations. In doing so, we compared wind speed at two heights (120 and 150 m), extracted at the five locations P1, P2, P3, P4, and WFA, from both the domains (which are illustrated in Fig. 2), spanning for 1 year from 01 to 07-2011 to 01-07-2012, and the results are illustrated in Fig. 6.

The bivariate histograms clearly show that the wind speeds are perfectly aligning along the one-to-one line, with a Pearson's correlation coefficient ranging between 0.96 and 0.98, implying a better agreement between the two datasets. In addition, the RMSE scores are marginally differed, with 0.01 m/s at P1, 0.02 m/s at P2, 0.1 m/s at P3, 0.03 m/s at P4, and 0.07, which corroborates the better agreement between the two datasets. Upon a close inspection, it is observed that

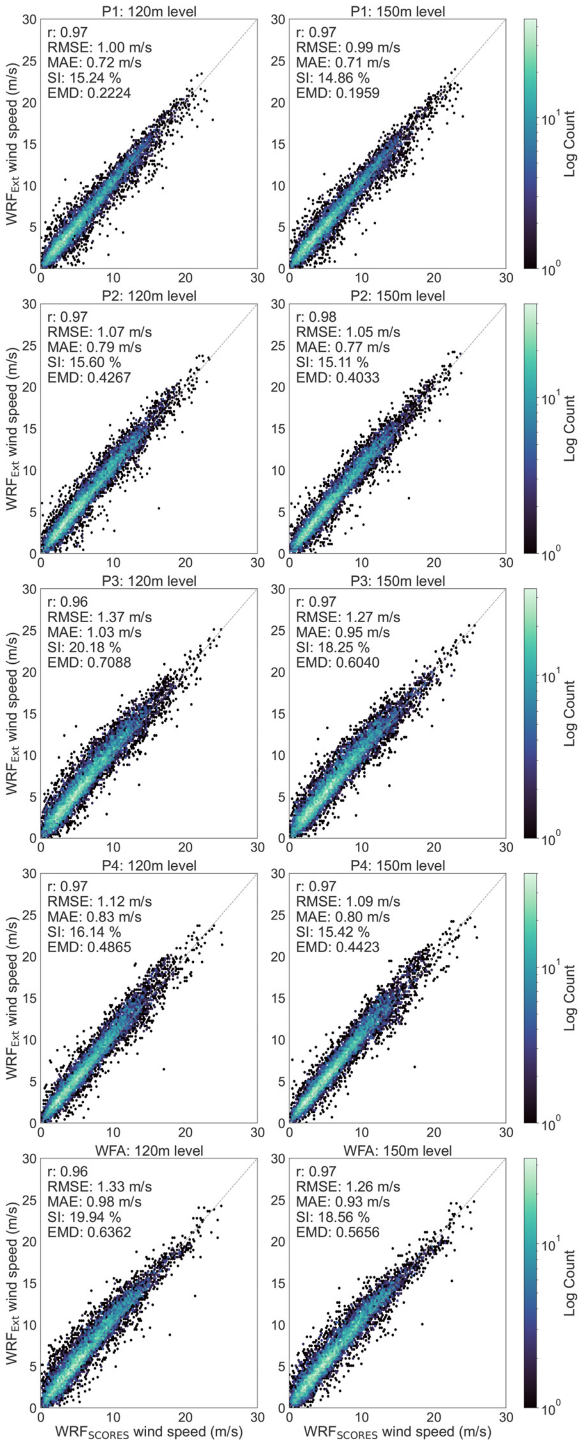

FIG. 6. Bivariate histograms depicting the 120 m (column 1) and 150 m (column 2) wind speed distributions from WRF$_{SCORES}$ and WRF$_{Ext}$ simulations, at points P1 (row 1), P2 (row 2), P3 (row 3), P4 (row 4), and WFA (row 5), during the period from 01-07-2011 to 01-07-2012, covering a year-long duration. The evaluation statistics (RMSE, r, MAE, SI, and the EMD) are computed to assess the agreement between the two datasets.

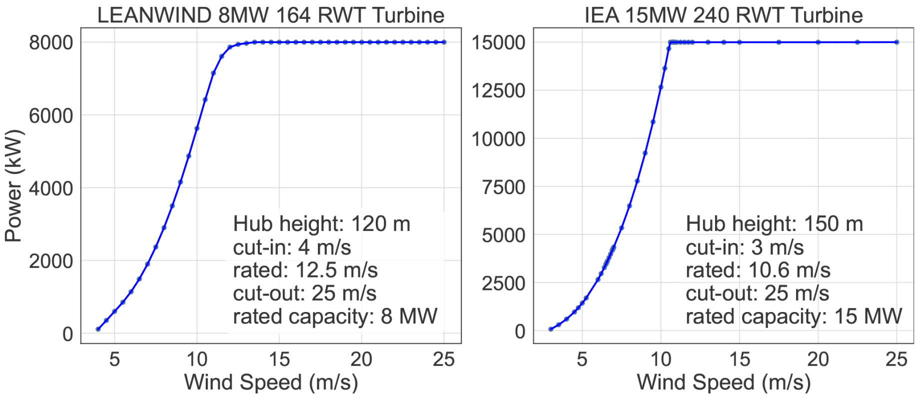

FIG. 7. Power curves of the LEANWIND 8 MW-164-RWT turbine (left) and IEA 15 MW-240-RWT turbine (right). The solid circles represent the manufacturer power curve, while the solid line represents the spline approximation.

the histograms have thinner spread at the sample points P1 and P2, while the spread is little higher at points P3 and WFA. The same is quantified through the scatter index, which is seen to be around 15% at P1 and P2, while the same is around 20% at P3 and WFA. These deviations lead to the marginal differences seen in terms of RMSE, MAE, and EMD. More specifically, the EMD is seen to be the least at P1, while the same is gradually increased as moving away from the coast, with P3 being the highest. Though a pattern is observed such as moving away from the coast resulted increasing differences, the differences are marginal. In Sec. III A, the validity of the wind dataset from the WRF$_{\text{Ext}}$ simulations was quantified and was found to be comparable with respect to observations as well as other reanalysis through intermediate comparison. Given the similarity of the WRF$_{\text{Ext}}$ and WRF$_{\text{SCORES}}$ results, we contend that the WRF$_{\text{SCORES}}$ setup can be used in full scale wind resource assessment.

IV. WIND RESOURCE ASSESSMENT

By utilizing the WRF$_{\text{SCORES}}$ domain, we generate a 31-year long wind dataset for a robust wind resource assessment. To align with real-world conditions, we employ established wind turbine models in wind energy estimation. The WindFloat Atlantic (WFA) offshore wind farm in our area of interest utilizes the MHI-Vestas V164-8.4 MW turbine, featuring a 164 m rotor diameter, 125 m hub height, and a rated capacity of 8.4 MW. As the power curve for this model is unavailable, we adopt the LEANWIND 8 MW-164-RWT turbine power curve,[53] which shares similar specifications. Additionally, for a comprehensive analysis, we incorporate the IEA 15 MW-240-RWT turbine model[54] to explore future wind energy production capabilities. The power curves of both turbines as a function of wind speed along with the necessary turbine specifications are illustrated in Fig. 7. To estimate the turbine power output P_t, we followed a similar methodology adopted in windpowerlib,[55] such that, a spline approximation is first made with the turbine power curve, then the power output is estimated corresponding to the wind speed at the hub height. Needless to say, the power outputs are capped at cut-in and cutout wind speeds. For reference, the spline approximations of power curves are also presented in Fig. 7 as solid line. This method allows one to estimate wind power output at every time instance, making it possible for analysis at all time-scales.

Once the turbine power is estimated, the power is normalized by the rated power (P_r) to define the instantaneous capacity factor CF as

$$CF = \frac{P_t}{P_r}. \tag{2}$$

This allows the analysis to be performed independently of the magnitude of the power of the reference wind turbine and can be scaled by future installed farm capacity where required.[56] A similar methodology has been adopted by many researchers in analyzing the wind resources at various time scales.[57–59] With the CF values having in hand, to find total energy (MWh) output in a single hour, one would simply multiply the hour's CF by the rated power (MW) and by 1 h[59] as

$$E_t = CF \times P_r \times 1 \quad (\text{MWh}). \tag{3}$$

Subsequently, the Annual Energy Production (AEP) can be computed during 1 year period in terms of mean CF as

$$AEP = n \times \overline{CF} \times P_r \times 1 \quad (\text{MWh}). \tag{4}$$

Here, n is the number of hours in a given 1 year period.

A. Wind resource assessment and pattern identification

Figure 8 illustrates the mean wind resources averaged over a 31-year period, such as mean wind speed and mean capacity factor, at the turbine height levels 120 and 150 m. In a larger context, the mean resources are seen to be varying with respect to distance from the coast, as well as with respect to change in height level (associated with rated capacity of turbines). Mean wind speed at 120 m level is ranging between < 7 m/s (near shore) and 7.7 m/s (far shore), while at 150 m level is ranging between 7 m/s (near shore) and 7.9 m/s (far shore). On the other hand, the capacity factor at 120 m and from the 8 MW turbine model is ranging between $< 35\%$ (near shore) to 39% (far shore), while the same at 150 m level and from 15 MW turbine model is ranging between 35% (ner shore) and 45% (far shore). Considering a wind farm located at the maximum CF region, the average AEP from the 8 MW turbine during 31 years would be 27.61 GWh, while the same from the 15 MW turbine would be 58.70 GWh, which is 112% higher than the previous. Similarly in order to examine the spatial advantage within the domain, consider a wind farm located 1 km near to the coast while another at the maximum CF region some where around 30 km away from the coast. There exist a 4% difference in mean CF for 8 MW turbine model, which results a 2.8 GWh difference in AEP. On

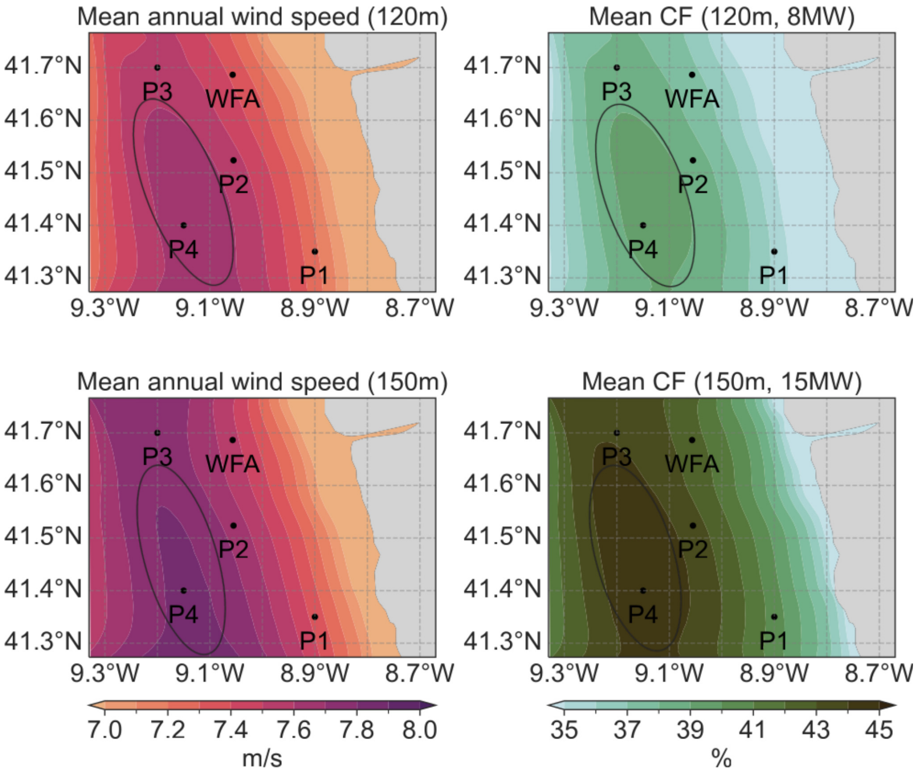

FIG. 8. Surface plots illustrating wind speed (column 1) and capacity factor (column 2) averaged over a 31-year period (from 01-01-1990 to 01-01-2021), at the turbine height levels 120 m (row 1) and 150 m (row 2). The capacity factors are estimated using the 8 MW turbine model at 120 m level and the 15 MW turbine model at 150 m level. The solid ellipses illustrated in each subplot represent the tongue-like resource maxima, which discussed further in the text.

the contrary, a 10% difference is observed for the 15 MW turbine model, which results a 13.14 GWh difference in AEP. From these, it is clearly evident that moving farther from the coast and adopting the 15 MW turbine model have significant advantage compared to the near shore location and 8 MW turbine model, in terms of power production.

A qualitative assessment is conducted at the five points: P1, P2, P3, P4, and WFA, which are roughly away from the coast by 11, 22, 28, 30, and 20 km, respectively. The 31-year mean CF and mean AEP are estimated at these points, and are presented in Table IV. Among these points, P1 is having least mean CF value, while the P4 is having highest. For the 8 MW turbine model, the CF changes by 3% by moving from the near-shore point P1 to far-shore point P4, which results in a difference of 2.52 GWh AEP. Similarly, for the 15 MW turbine model, moving from P1 to P4 results 4% change in CF and 5.37 GWh

TABLE IV. Mean CF and average AEP at different locations over a 31-year period.

	120 m, 8 MW		150 m, 15 MW	
Location	Mean CF (%)	AEP (GWh)	Mean CF (%)	AEP (GWh)
P1	36.0	25.11	41.0	53.32
P2	38.0	27.00	43.0	57.09
P3	38.0	26.87	44.0	57.68
P4	39.0	27.61	45.0	58.70
WFA	37.0	26.14	42.0	55.74

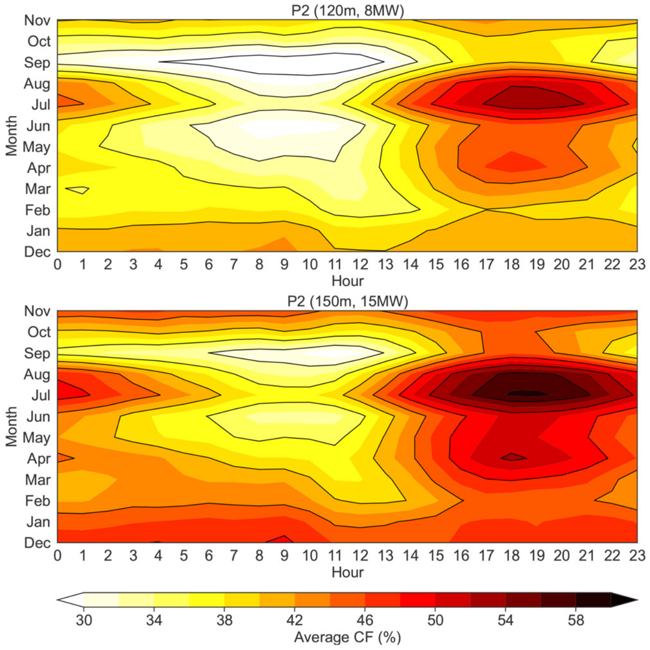

FIG. 9. Contours of combined diurnal and annual variability of mean CF values at point P2. Hourly values of CF are sampled by conditioning respective to each month and averaged over a 31-year period (from 01-01-1990 to 01-01-2021). Top row depicting the variability from the 8 MW turbine model while the bottom row depicting the variability from 15 MW turbine model.

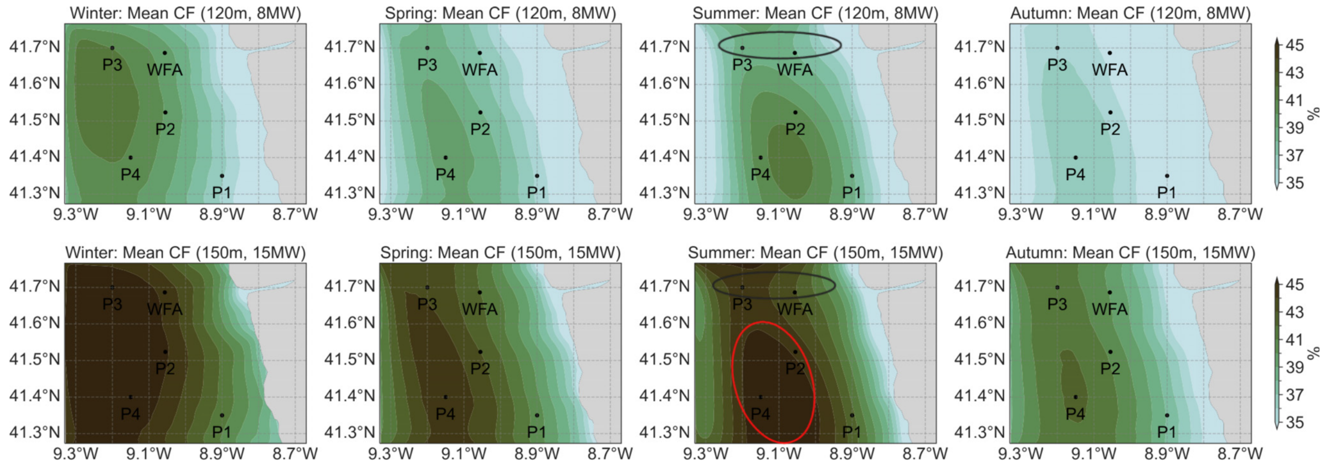

FIG. 10. Surface plots illustrating seasonal mean capacity factors during Winter (DJF) (column 1), Spring (MAM) (column 2), Summer (JJA) (column 3), and Autumn (SON) (column 4) months. The capacity factors are estimated using the turbine models: 8 MW and 120 m wind speed (row 1) and 15 MW and 150 m wind speed (row 2). The solid ellipses illustrated in the third column subplots represent the neck-like contraction, which is further discussed in the text. The red ellipse holds similar reasoning seen in Fig. 8.

in AEP. Though the gain in CF seems marginal (3%–4%) by moving 19 km further offshore, the quantitative gain in the AEP does have significant implications on cost analysis. On the contrary, moving from the existing WFA location to P4 results 2% change in CF and 1.47 GWh in AEP for the 8 MW turbine model, whereas, 3% change in CF and 2.96 GWh in AEP for the 15 MW turbine model. These finding suggest that a careful examination of climatology is of paramount importance before full scale deployment of wind farms.

A closer examination of the mean wind resources depicted in Fig. 8 reveals a distinctive tongue-like pattern of maxima running parallel to the coastline (represented by solid ellipses in each subplot). This characteristic points toward the influence of an underlying weather phenomenon associated with coastal effects. To further understand its characteristics, we plotted the combined diurnal-annual cycle of CF at point P2, from both turbine models, as shown in Fig. 9. It turns out that the weather phenomenon has a strong diurnal pattern and seasonal dependence. The diurnal trend of CF increasing post afternoon and reaching maxima at 1800UTC is persisting during spring to autumn seasons, with an intensification during summer. Based on past studies,[60–62] we recognize that IPCJ is the underlying weather phenomenon responsible for the observed wind maxima. Coastal jets are primarily a consequence of the thermal contrast between warm land and cold ocean; the resulting coast-parallel winds are the geostrophically adjusted response to the thermal gradient and Coriolis deflection.[63] Ranjha *et al.*[60] first identified the existence of IPCJ, occurring only during summer months (JJA), which is related to the presence of Azores High in the Northern Atlantic during this period, which gives rise to the coast-parallel flow and consequently coastal low-level jet. Soares *et al.*[61] further examined the seasonality of the IPCJ and found that the frequency of occurrence of coastal jets is 10%–12% during Spring months (MAM), increases to 30% during Summer (JJA), and then decreases to 8%–10% by Autumn (SON).

To further support our claim that the IPCJ are, indeed, the source of tongue-like wind resource maxima along the coast, we analyzed the seasonal maps of mean capacity factor from the two turbine power curves, as shown in Fig. 10. From the maps, it is evident that a tongue-like maxima persist during Spring, Summer, and Autumn seasons, with more pronounced during Summer (red ellipse), which is confirming that the IPCJ is responsible for the intensified wind and capacity factor maxima. Though the capacity factor is generally high during Winter months, they are not associated with the coastal jets, but with easterly winds from land, and has different dynamics (cold land and warm ocean), falling more into the katabatic flow category.[61] Overall, the mean capacity factor seen highest during Winter, decreasing slightly during Spring, then reaching peak again during Summer, then falling to minimum during Autumn.

An interesting neck-like contraction pattern (around 41.7N latitude) is found during summer mean CF, while a weak one during the spring and autumn maps (represented by the solid black ellipses in Fig. 10 third column). When the coast-parallel flow interacts with points and capes at the coast, gravity waves are excited. These gravity waves propagate on the marine atmospheric boundary layer inversion and are responsible for the adjustment of the flow that leads to changes in the wind speed and direction in the lee of the headlands. The flow becomes supercritical (subcritical) if the gravity waves have a phase speed that is lower (higher) than the wind speed. If the coast opens away from the flow, in the lee of the headland, and the flow is supercritical, an expansion fan develops. This expansion fan is responsible for the turn of the wind direction toward the coast, and for the decrease in the MABL height, leading to an increase in the wind speed through a Bernoulli effect.[62] Though the cape (41.73N, 8.9W) seems really small compared to the one mentioned in Rijo *et al.*,[62] it does seem have an impact on the intensity of IPCJ very close to the coast. In our context of suitable location for maximum wind power potential, the existing WindFloat Atlantic wind farm exactly located in the neck region, making it relatively less suitable, compared to points P2 or P4, which situated in the expansion fan region. This actually explains the marginal differences seen in mean CF earlier. We can confidently assert that this discovery is possible through the use of gray-zone resolution simulations, implying the significance of our dataset, and the need for high-fidelity resource assessments.

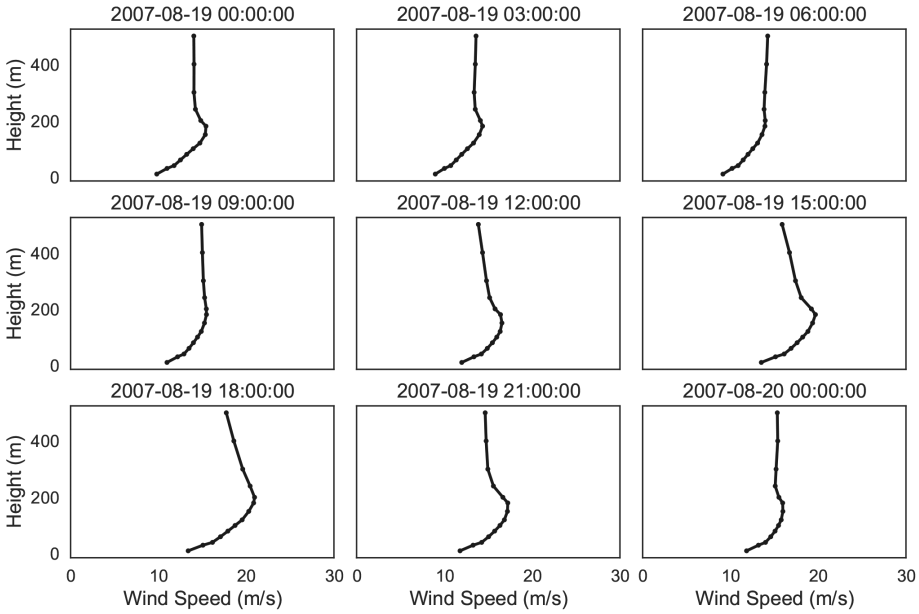

FIG. 11. Vertical profiles of simulated wind speed at point P2, during 19th of August 2007.

Earlier studies[60,61] reported that the maximum wind speed in the vertical profile of the IPCJ (core height) is around 400 m. However, our analysis for the same day (19 August of 2007) showed that the core height is well below 200 m height (Fig. 11), which is very close to the turbine hub height. This means winds increase drastically from surface to the jet height, significantly amplifying the wind power potential at higher altitudes up to the jet core height. The same is evident in the significantly higher capacity factor from the 15 MW turbine model and 150 m winds, compared to the 8 MW turbine. One possible reason for the increased jet core height is the increase in horizontal and vertical resolutions of the model simulations.

B. Resource variability

To examine the resource variability across diurnal and annual time-scales, we plotted the mean CF values at the five points, averaged over the respective time-scales, as shown in Fig. 12. The plots also depict the variability within the wind speed level and turbine models adopted in this study. From this figure, it is clear that the capacity factors have well defined diurnal cycle, with minimum CF occurring around 1100UTC and maximum occurring around 1800UTC. Similarly, the CF values also show an annual variability, reaching maximum during July and minimum during September. These variability cycles are exactly aligning with the occurrence of IPCJ, reported in earlier studies,[61,62] confirming that the IPCJ are the major player in deciding the wind resources in our domain of interest. Needless to say, the CF values from the 15 MW turbine model are 5% higher compared to its counterpart, at each location, implying the advantage by adopting advanced turbine model solely in terms of power produced.

In the diurnal cycle, during 0000UTC to 1400UTC, the capacity factor values are in the increasing order of P1, WFA, P2, P3, and P4, which is indeed seen in Table IV. However, right after this time and until 2000UTC, the capacity factor values at P1, P2, and P4 reach higher than the P3 and WFA, which is exactly inline with the previous

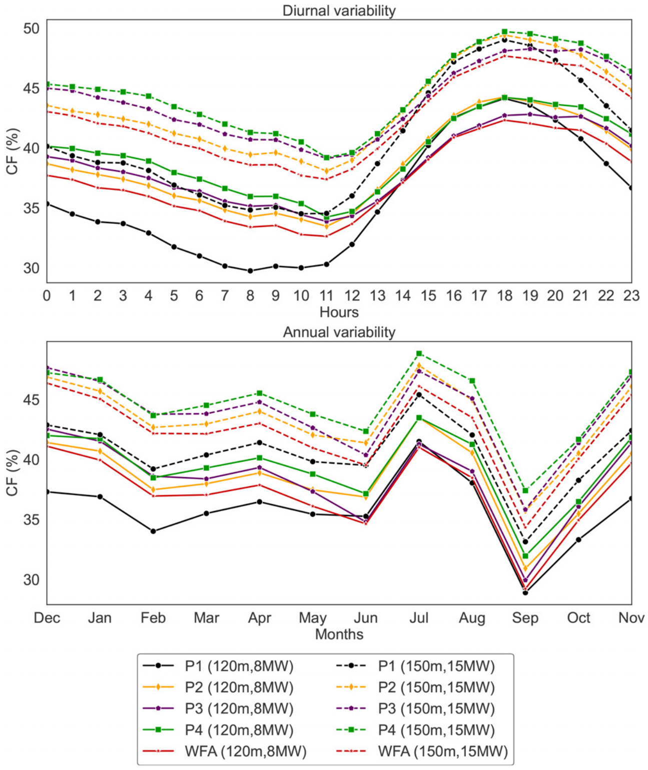

FIG. 12. Time-series plots illustrating the variability of mean CF over a 31-year period (from 01-01-1990 to 01-01-2021), averaged over every hour (first row) depicting diurnal variability and averaged over every month (second row) depicting annual variability. Each plot depicting CF values from 120 m wind speed and 8 MW turbine model (solid lines) and from 150 m wind speed and 15 MW turbine model (dashed lines), at points P1, P2, P3, P4, and WFA.

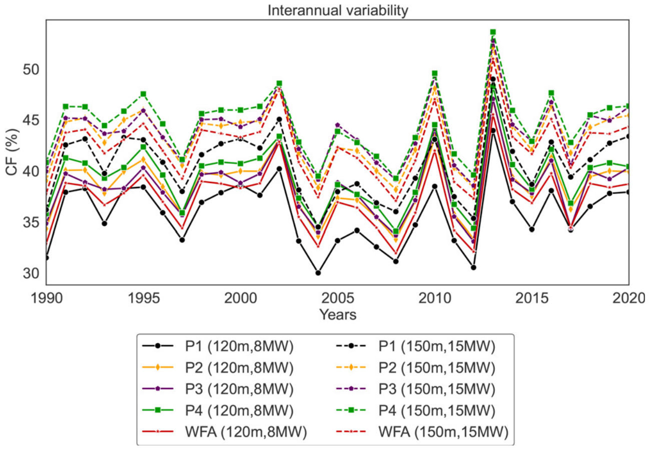

FIG. 13. Time-series plot illustrating the variability of mean CF over a 31-year period (from 01-01-1990 to 01-01-2021), averaged over every year depicting interannual variability. Each plot depicting CF values from 120 m wind speed and 8 MW turbine model (solid lines) and from 150 m wind speed and 15 MW turbine model (dashed lines), at points P1, P2, P3, P4, and WFA.

analogy of cape interaction resulted in neck-like contraction. After 2000UTC, again the capacity factor values decrease and come to their previous trend. A similar trend is seen in the annual cycle as well. The capacity factor values are in the increasing order of P1, WFA, P2, P3, and P4, from December to May. Right during the peak summer time (JJA), the CF values at P1, P2, and P4 reach higher than the P3 and WFA. From both of these cycles, and from Fig. 10, it is further confirmed that the neck-like contraction is a phenomenon associated with the IPCJ, which does have significant influence on the wind power potential.

Finally, the interannual variability of capacity factors at the five locations and from both the turbine models is depicted in Fig. 13. The mean CF values at all locations are seen to be the highest during 2013, while least during 2004 and 2012. During all years, the mean CF at P4 are seen to be the highest among all points, while at P1 being the lowest. Furthermore, a consistent difference of 4%–6% is observed between these two locations during all years, for the 8 MW turbine model as well as the 15 MW turbine model, which is in line with the findings from previous sections. In addition, there exists a consistent difference of 10% between the mean CF at P1 from the 8 MW turbine and the mean CF at P4 from the 15 MW turbine models, which is also inline with the findings from previous sections. These findings corroborate the conclusion that the P4 locations as the maximum CF yielding while the 15 MW turbine model as the best suitable model. Apart from these, a more interesting observations is that the difference in mean CF values between 2012 and 2013 years at all respective points is roughly 15%. This difference accounts for a change of 10.5 GWh AEP for the 8 MW turbine model and 19.7 GWh AEP for the 15 MW model. Estimation of such interannual fluctuations allows one to accurately design the wind farms to extract maximum wind energy that is available.

While acknowledging the substantial impact of teleconnections such as the North Atlantic Oscillation, East Atlantic, and Scandinavian modes on wind resources, this study refrains from an in-depth analysis of these influences. Recent research[64–66] has comprehensively explored the intricate interplay between large-scale circulation patterns and wind power potential in the Iberian Peninsula. However, the current work deliberately focuses on a detailed examination of local wind resource variabilities, leaving a comprehensive investigation of broader teleconnections for future research endeavors.

V. CONCLUSIONS

In conclusion, the comprehensive analysis of wind speed distributions at various observational locations along the Portuguese coast highlights the significant role of the WRF simulations at 500 m resolution, in providing reliable and accurate representations of observed wind patterns. While ERA5 and CERRA exhibit notable discrepancies, the WRF simulations consistently demonstrate improved performance in capturing the complexity of wind speed distributions. This superiority is evident in reduced biases, closer alignment with observed distributions, and lower Earth Mover's Distance values.

Furthermore, our comprehensive wind resource assessment, utilizing the 31-year wind dataset, reveals valuable insight of coastal effects on offshore wind energy production along the Portugal coast. By adopting established wind turbine power curves, such as the MHI-Vestas V164-8.4 MW and IEA 15 MW-240-RWT, we estimated turbine power output and subsequently normalized it to define the capacity factor (CF). The mean wind resources exhibit distinct variations with proximity to the coast and changes in turbine hub-height levels. The presence of IPCJ is identified as a key factor influencing wind maxima, particularly during Spring, Summer, and Autumn seasons. Spatially, points situated further offshore demonstrate higher CF values, emphasizing the significance of location in wind farm planning. The diurnal and annual variability in CF aligns with the IPCJ occurrence, highlighting its impact on wind power potential. Our findings underscore the importance of considering climatology and turbine power curve selection for optimizing wind farm deployment, with potential implications for energy production and cost analysis. Overall, this study provides valuable insight into the dynamics of wind resources in the Portugal coast region, supporting informed decision-making for sustainable offshore wind energy projects.

The generated wind dataset can be utilized in various follow-up projects. This includes, but is not limited to, investigating the impact of teleconnection indices on wind resources. Moreover, the dataset provides a foundation for characterizing extreme events, such as wind ramps, at sub-hourly time scales. Additionally, wind turbine wakes are one of the most important aspects of wind power meteorology because they decrease the power production and increase the loading of downstream wind turbines.[67,68] A horizontal resolution of a few hundred meters is needed to place each turbine of a wind farm in individual cells and account for intra-farm wake effects.[69] We believe that the WRF model-generated data at a gray-zone resolution of 500 m could be very valuable for wake calculations and offers an opportunity to delve deeper into understanding both intra-farm and farm-to-farm wake losses. These avenues for further research will contribute to the growing field of offshore wind energy research.

ACKNOWLEDGMENTS

The authors acknowledge the use of computational resources of DelftBlue supercomputer, provided by Delft High Performance Computing Centre (https://www.tudelft.nl/dhpc). We thank SURF (www.surf.nl) for the support in using the National Supercomputer

Snellius. The work was part of the EU-SCORES project from the European Union's Horizon 2020 research and innovation programme under Grant Agreement No. 101036457.

AUTHOR DECLARATIONS

Conflict of Interest

The authors have no conflicts to disclose.

Author Contributions

H. Baki: Conceptualization (equal); Data curation (equal); Formal analysis (equal); Investigation (equal); Methodology (equal); Writing – original draft (equal). **S. Basu:** Supervision (equal); Writing – review & editing (equal). **G. Lavidas:** Supervision (equal); Writing – review & editing (equal).

DATA AVAILABILITY

The CERRA and ERA5 reanalysis datasets have been used for driving the WRF model simulations are publicly available in Climate Data Store at https://doi.org/10.24381/cds.a39ff99f (Ref. 21), https://doi.org/10.24381/cds.622a565a (Ref. 70), and https://doi.org/10.24381/cds.adbb2d47 (Ref. 71). Upon publication, the processed data used to create the figures will be made available in Zenodo at https://doi.org/10.5281/zenodo.13987308 (Ref. 72). The raw WRF-generated data are available from the corresponding author upon reasonable request.

REFERENCES

[1] European Union, see https://eur-lex.europa.eu/eli/dir/2018/2001/oj for "Directive (EU) 2018/2001 of the European Parliament and of the Council of 11 December 2018 on the promotion of the use of energy from renewable sources" (2018); accessed 18 October 2023.

[2] New Atlas, see https://newatlas.com/energy/worlds-largest-wind-turbine-myse-16-260/ for "World's largest wind turbine to feature 16 mw capacity" (2024); accessed 23 March 2024.

[3] Y. Guo, H. Wang, and J. Lian, "Review of integrated installation technologies for offshore wind turbines: Current progress and future development trends," Energy Convers. Manage. **255**, 115319 (2022).

[4] M. Vieira, E. Henriques, M. Amaral, N. Arantes-Oliveira, and L. Reis, "Path discussion for offshore wind in Portugal up to 2030," Mar. Policy **100**, 122–131 (2019).

[5] Wind Europe, see https://windeurope.org/intelligence-platform/product/offshore-wind-energy-2023-mid-year-statistics for "Offshore wind energy 2023 mid-year statistics" (2023); accessed 18 October 2023.

[6] N. Salvação and C. Guedes Soares, "Resource assessment methods in the offshore wind energy sector," in *Floating Offshore Wind Farms. Green Energy and Technology* (Springer, 2016), pp. 121–141.

[7] M. A. Prósper, C. Otero-Casal, F. C. Fernández, and G. Miguez-Macho, "Wind power forecasting for a real onshore wind farm on complex terrain using WRF high resolution simulations," Renewable Energy **135**, 674–686 (2019).

[8] C. G. Nunalee and S. Basu, "Mesoscale modeling of coastal low-level jets: Implications for offshore wind resource estimation," Wind Energy **17**, 1199–1216 (2014).

[9] C. Steele, S. Dorling, R. von Glasow, and J. Bacon, "Modelling sea-breeze climatologies and interactions on coasts in the Southern North Sea: Implications for offshore wind energy," Q. J. R. Meteorol. Soc. **141**, 1821–1835 (2015).

[10] M. Dörenkämper, B. Witha, G. Steinfeld, D. Heinemann, and M. Kühn, "The impact of stable atmospheric boundary layers on wind-turbine wakes within offshore wind farms," J. Wind Eng. Ind. Aerodyn. **144**, 146–153 (2015).

[11] J. Schulz-Stellenfleth, S. Emeis, M. Dörenkämper, J. Bange, B. Cañadillas, T. Neumann, J. Schneemann, I. Weber, K. Zum Berge, A. Platis *et al.*, "Coastal impacts on offshore wind farms—A review focussing on the German bight area," Meterol. Z. **31**, 289–315 (2022).

[12] R. Guanche, C. Vidal, A. Piedra, and I. Losada, "IDERMAR METEO. Offshore wind assessment at high and very high water depths," in *OCEANS 2011 IEEE-Spain* (IEEE, 2011), pp. 1–8.

[13] A. Estanqueiro, A. Couto, L. Rodrigues, and R. Marujo, "Wind resource assessment method for floating deep offshore wind turbines," IET Eng. Technol. Ref. **1**, 7 (2014).

[14] C.-D. Yue, Y.-S. Chiu, C.-C. Tu, and T.-H. Lin, "Evaluation of an offshore wind farm by using data from the weather station, floating LiDAR, Mast, and MERRA," Energies **13**, 185 (2020).

[15] Y. L. Pichugina, R. M. Banta, W. A. Brewer, S. P. Sandberg, and R. M. Hardesty, "Doppler Lidar–based wind-profile measurement system for offshore wind-energy and other marine boundary layer applications," J. Appl. Meteorol. Climatol. **51**, 327–349 (2012).

[16] G. Gualtieri, "Analysing the uncertainties of reanalysis data used for wind resource assessment: A critical review," Renewable Sustainable Energy Rev. **167**, 112741 (2022).

[17] D. P. Dee, S. M. Uppala, A. J. Simmons, P. Berrisford, P. Poli, S. Kobayashi, U. Andrae, M. Balmaseda, G. Balsamo, d P. Bauer *et al.*, "The era-interim reanalysis: Configuration and performance of the data assimilation system," Q. J. R. Meteorol. Soc. **137**, 553–597 (2011).

[18] R. Gelaro, W. McCarty, M. J. Suárez, R. Todling, A. Molod, L. Takacs, C. A. Randles, A. Darmenov, M. G. Bosilovich, R. Reichle *et al.*, "The modern-era retrospective analysis for research and applications, version 2 (MERRA-2)," J. Clim. **30**, 5419–5454 (2017).

[19] H. Hersbach, B. Bell, P. Berrisford, S. Hirahara, A. Horányi, J. Muñoz-Sabater, J. Nicolas, C. Peubey, R. Radu, D. Schepers *et al.*, "The ERA5 global reanalysis," Q. J. R. Meteorol. Soc. **146**, 1999–2049 (2020).

[20] M. I. Chidean, A. J. Caamaño, J. Ramiro-Bargueño, C. Casanova-Mateo, and S. Salcedo-Sanz, "Spatio-temporal analysis of wind resource in the Iberian Peninsula with data-coupled clustering," Renewable Sustainable Energy Rev. **81**, 2684–2694 (2018).

[21] S. Schimanke, M. Ridal, P. Le Moigne, L. Berggren, P. Undén, R. Randriamampianina, U. Andrea, E. Bazile, T. Bertelsen, P. Brousseau, P. Dahlgren, L. Edvinsson, A. E. Said, M. Glinton, S. Hopsch, L. Isaksson, R. Mladek, E. Olsson, A. Verrelle, and Z. Wang (2021). "CERRA sub-daily regional reanalysis data for Europe on pressure levels from 1984 to present," Dataset, Copernicus Climate Change Service (C3S) Climate Data Store (CDS).

[22] D. Carvalho, A. Rocha, and M. Gómez-Gesteira, "Ocean surface wind simulation forced by different reanalyses: Comparison with observed data along the Iberian Peninsula Coast," Ocean Modell. **56**, 31–42 (2012).

[23] D. Carvalho, A. Rocha, M. Gómez-Gesteira, and C. S. Santos, "Comparison of reanalyzed, analyzed, satellite-retrieved and NWP modelled winds with buoy data along the Iberian Peninsula Coast," Remote Sens. Environ. **152**, 480–492 (2014).

[24] D. Carvalho, A. Rocha, M. Gómez-Gesteira, and C. S. Santos, "Offshore wind energy resource simulation forced by different reanalyses: Comparison with observed data in the Iberian Peninsula," Appl. Energy **134**, 57–64 (2014).

[25] D. Carvalho, A. Rocha, M. Gómez-Gesteira, and C. S. Santos, "Offshore winds and wind energy production estimates derived from ASCAT, OSCAT, numerical weather prediction models and buoys–A comparative study for the Iberian Peninsula Atlantic Coast," Renewable Energy **102**, 433–444 (2017).

[26] D. Carvalho, A. Rocha, M. Gómez-Gesteira, and C. S. Santos, "Sensitivity of the WRF model wind simulation and wind energy production estimates to planetary boundary layer parameterizations for onshore and offshore areas in the Iberian Peninsula," Appl. Energy **135**, 234–246 (2014).

[27] N. Salvação and C. Guedes Soares, "Wind resource assessment offshore the Atlantic Iberian Coast with the WRF model," Energy **145**, 276–287 (2018).

[28] A. Claro, J. A. Santos, and D. Carvalho, "Assessing the future wind energy potential in Portugal using a CMIP6 model ensemble and WRF high-resolution simulations," Energies **16**, 661 (2023).

[29] S. M. Plecha, A. Teles-Machado, R. Tomé, and P. Mateus, "Offshore wind data assessment near the Iberian Peninsula over the last 25 years," Environ. Res.: Clim. **2**, 025008 (2023).

[30] A. Couto, J. Silva, P. Costa, D. Santos, T. Simões, and A. Estanqueiro, "Towards a high-resolution offshore wind Atlas-the Portuguese Case," J. Phys.: Conf. Ser. **1356**, 012029 (2019).

[31] Y. Takeyama, T. Ohsawa, J. Tanemoto, S. Shimada, K. Kozai, and T. Kogaki, "A comparison between advanced scatterometer and weather research and forecasting wind speeds for the Japanese offshore wind resource map," Wind Energy **23**, 1596–1609 (2020).

[32] J. C. Wyngaard, "Toward numerical modeling in the 'Terra Incognita'," J. Atmos. Sci. **61**, 1816–1826 (2004).

[33] J. C. Wyngaard, *Turbulence in the Atmosphere* (Cambridge University Press, 2010).

[34] H. H. Shin and S.-Y. Hong, "Analysis of resolved and parameterized vertical transports in convective boundary layers at gray-zone resolutions," J. Atmos. Sci. **70**, 3248–3261 (2013).

[35] H. H. Shin and S.-Y. Hong, "Representation of the subgrid-scale turbulent transport in convective boundary layers at gray-zone resolutions," Mon. Weather Rev. **143**, 250–271 (2015).

[36] R. Honnert, G. A. Efstathiou, R. J. Beare, J. Ito, A. Lock, R. Neggers, R. S. Plant, H. H. Shin, L. Tomassini, and B. Zhou, "The atmospheric boundary layer and the 'gray zone' of turbulence: A critical review," JGR Atmos. **125**, e2019JD030317 (2020).

[37] P. A. Jiménez, J. Navarro, A. M. Palomares, and J. Dudhia, "Mesoscale modeling of offshore wind turbine wakes at the wind farm resolving scale: A composite-based analysis with the Weather Research and Forecasting model over Horns Rev," Wind Energy **18**, 559–566 (2015).

[38] W. C. Skamarock, J. B. Klemp, J. Dudhia, D. O. Gill, Z. Liu, J. Berner, W. Wang, J. G. Powers, M. G. Duda, D. M. Barker *et al.*, "A description of the advanced research WRF version 4," NCAR Technical Note NCAR/TN-556+STR 145, 2019.

[39] H. Baki, S. Basu, and G. Lavidas, "Modelling frontal low-level jets and associated extreme wind power ramps over the North Sea," Wind Energy Sci. Discuss. (published online) (2024).

[40] M. J. Iacono, J. S. Delamere, E. J. Mlawer, M. W. Shephard, S. A. Clough, and W. D. Collins, "Radiative forcing by long-lived greenhouse gases: Calculations with the AER radiative transfer models," J. Geophys. Res. **113**, D13103, https://doi.org/10.1029/2008JD009944 (2008).

[41] P. A. Jiménez, J. Dudhia, J. F. González-Rouco, J. Navarro, J. P. Montávez, and E. García-Bustamante, "A revised scheme for the WRF surface layer formulation," Mon. Weather Rev. **140**, 898–918 (2012).

[42] N. Mukul Tewari, M. Tewari, F. Chen, W. Wang, J. Dudhia, M. LeMone, K. Mitchell, M. Ek, G. Gayno, J. Wegiel *et al.*, "Implementation and verification of the unified NOAH land surface model in the WRF model (formerly paper number 17.5)," in *Proceedings of the 20th Conference on Weather Analysis and Forecasting/16th Conference on Numerical Weather Prediction*, Seattle, WA (2004), Vol. 14.

[43] S.-Y. Hong, J. Dudhia, and S.-H. Chen, "A revised approach to ice microphysical processes for the bulk parameterization of clouds and precipitation," Mon. Weather Rev. **132**, 103–120 (2004).

[44] T. Remmers, F. Cawkwell, C. Desmond, J. Murphy, and E. Politi, "The potential of advanced scatterometer (ASCAT) 12.5 km coastal observations for offshore wind farm site selection in Irish waters," Energies **12**, 206 (2019).

[45] L. Mahrt, D. Vickers, E. L. Andreas, and D. Khelif, "Sensible heat flux in near-neutral conditions over the sea," J. Phys. Oceanogr. **42**, 1134–1142 (2012).

[46] J. Olauson, "ERA5: The new champion of wind power modelling?" Renewable Energy **126**, 322–331 (2018).

[47] J. Ramon, L. Lledó, V. Torralba, A. Soret, and F. J. Doblas-Reyes, "What global reanalysis best represents near-surface winds?" Q. J. R. Meteorol. Soc. **145**, 3236–3251 (2019).

[48] D. Carvalho, A. Rocha, M. Gómez-Gesteira, and C. Santos, "A sensitivity study of the WRF model in wind simulation for an area of high wind energy," Environ. Modell. Software **33**, 23–34 (2012).

[49] J. MacMahan, "Increased aerodynamic roughness owing to surfzone foam," J. Phys. Oceanogr. **47**, 2115–2122 (2017).

[50] Y. He, J. Fu, P. W. Chan, Q. Li, Z. Shu, and K. Zhou, "Reduced sea-surface roughness length at a coastal site," Atmosphere **12**, 991 (2021).

[51] N. Lupu, L. Selios, and Z. Warner, "A new measure of congruence: The Earth mover's distance," Polit. Anal. **25**, 95–113 (2017).

[52] A. N. Hahmann, T. Sīle, B. Witha, N. N. Davis, M. Dörenkämper, Y. Ezber, E. García-Bustamante, J. F. González-Rouco, J. Navarro, B. T. Olsen, and S. Söderberg, "The making of the new European wind atlas – Part 1: Model sensitivity," Geosci. Model Dev. **13**, 5053–5078 (2020).

[53] C. Desmond, J. Murphy, L. Blonk, and W. Haans, "Description of an 8 mw reference wind turbine," J. Phys.: Conf. Ser. **753**, 092013 (2016).

[54] E. Gaertner, J. Rinker, L. Sethuraman, F. Zahle, B. Anderson, G. Barter, N. Abbas, F. Meng, P. Bortolotti, W. Skrzypinski *et al.*, "Definition of the IEA 15-megawatt offshore reference wind turbine," Report No. NREL/TP-5000-75698, 2020.

[55] S. Haas, B. Schachler, and U. Krien (2019). "windpowerlib—A python library to model wind power," Zenodo V.0.2.0. https://doi.org/10.5281/zenodo.3403360

[56] P. Potisomporn and C. R. Vogel, "Spatial and temporal variability characteristics of offshore wind energy in the United Kingdom," Wind Energy **25**, 537–552 (2022).

[57] V. Ramos, G. Giannini, T. Calheiros-Cabral, M. López, P. Rosa-Santos, and F. Taveira-Pinto, "Assessing the effectiveness of a Novel WEC concept as a co-located solution for offshore wind farms," J. Mar. Sci. Eng. **10**, 267 (2022).

[58] S. Pryor, F. Letson, and R. Barthelmie, "Variability in wind energy generation across the contiguous United States," J. Appl. Meteorol. Climatol. **59**, 2021–2039 (2020).

[59] D. Millstein, S. Jeong, A. Ancell, and R. Wiser, "A database of hourly wind speed and modeled generation for US wind plants based on three meteorological models," Sci. Data **10**, 883 (2023).

[60] R. Ranjha, G. Svensson, M. Tjernström, and A. Semedo, "Global distribution and seasonal variability of coastal low-level jets derived from ERA-Interim reanalysis," Tellus Ser. A **65**, 20412 (2013).

[61] P. M. M. Soares, R. M. Cardoso, Á. Semedo, M. J. Chinita, and R. Ranjha, "Climatology of the Iberia coastal low-level wind jet: Weather research forecasting model high-resolution results," Tellus Ser. A **66**, 22377 (2014).

[62] N. Rijo, A. Semedo, P. M. A. Miranda, D. Lima, R. M. Cardoso, and P. M. M. Soares, "Spatial and temporal variability of the Iberian peninsula coastal low-level jet," Int. J. Climatol. **38**, 1605–1622 (2018).

[63] T. R. Parish, "Forcing of the summertime low-level jet along the California coast," J. Appl. Meteorol. **39**, 2421–2433 (2000).

[64] S. Jerez and R. M. Trigo, "Time-scale and extent at which large-scale circulation modes determine the wind and solar potential in the Iberian Peninsula," Environ. Res. Lett. **8**, 044035 (2013).

[65] S. Jerez, R. M. Trigo, S. M. Vicente-Serrano, D. Pozo-Vázquez, R. Lorente-Plazas, J. Lorenzo-Lacruz, F. Santos-Alamillos, and J. P. Montávez, "The impact of the North Atlantic oscillation on renewable energy resources in Southwestern Europe," J. Appl. Meteorol. Climatol. **52**, 2204–2225 (2013).

[66] J. M. Correia, A. Bastos, M. C. Brito, and R. M. Trigo, "The influence of the main large-scale circulation patterns on wind power production in Portugal," Renewable Energy **102**, 214–223 (2017).

[67] J. S. Rodrigo, F. B. Guillén, P. M. F. Correia, B. G. Hevia, W. Schlez, S. Schmidt, S. Basu, B. Li, P. Nielsen, M. Cathelain *et al.*, "Validation of meso-wake models for array efficiency prediction using operational data from five offshore wind farms," J. Phys.: Conf. Ser. **1618**, 062044 (2020).

[68] F. Porté-Agel, M. Bastankhah, and S. Shamsoddin, "Wind-turbine and wind-farm flows: A review," Boundary-Layer Meteorol. **174**, 1–59 (2020).

[69] J. Fischereit, R. Brown, X. G. Larsén, J. Badger, and G. Hawkes, "Review of mesoscale wind-farm parametrizations and their applications," Boundary-Layer Meteorol. **182**, 175–224 (2022).

[70] S. Schimanke, M. Ridal, P. L. Moigne, L. Berggren, P. Undén, R. Randriamampianina, U. Andrea, E. Bazile, A. Bertelsen, P. Brousseau, P. Dahlgren, L. Edvinsson, A. E. Said, M. Glinton, S. Hopsch, L. Isaksson, R. Mladek, E. Olsson, A. Verrelle, and Z. Q. Wang (2021). "CERRA sub-daily

regional reanalysis data for Europe on single levels from 1984 to present," Dataset, Copernicus Climate Change Service (C3S) Climate Data Store (CDS). https://doi.org/10.24381/cds.622a565a

[71] H. Hersbach, B. Bell, P. Berrisford, G. Biavati, A. Horányi, J. Muño. Sabater, J. Nicolas, C. Peubey, R. Radu, I. Rozum, D. Schepers, A. Simmons, C. Soci, D. Dee, and J.-N. Thépaut (2023). "ERA5 hourly data on single levels from 1940 to present," Dataset, Copernicus Climate Change Service (C3S) Climate Data Store (CDS). https://doi.org/10.24381/cds.adbb2d47

[72] H. Baki, S. Basu, and G. Lavidas (2024). "Dataset for 'Estimating the offshore wind power potential of Portugal by utilizing gray-zone atmospheric modeling' article," Zenodo. https://doi.org/10.5281/zenodo.13987307